Introducing *ab initio* based neural networks for transition-rate prediction in kinetic Monte Carlo simulations

Luca Messina*
DEN–Service de Recherches de Métallurgie Physique, CEA, Université Paris-Saclay, F-91191 Gif-sur-Yvette, France

Nicolas Castin
Studie Centrum voor Kerneenergie, Centre d'Études de l'énergie Nucléaire (SCK·CEN), NMS unit, Boeretang 200, B2400, Mol, Belgium

Christophe Domain
Département Matériaux et Mécanique des Composants, EDF–R&D, Les Renardières, F-77250 Moret sur Loing, France

Pär Olsson
KTH Royal Institute of Technology, Reactor Physics, SE-106 91 Stockholm, Sweden
(Received 20 October 2016; published 27 February 2017)

The quality of kinetic Monte Carlo (KMC) simulations of microstructure evolution in alloys relies on the parametrization of point-defect migration rates, which are complex functions of the local chemical composition and can be calculated accurately with *ab initio* methods. However, constructing reliable models that ensure the best possible transfer of physical information from *ab initio* to KMC is a challenging task. This work presents an innovative approach, where the transition rates are predicted by artificial neural networks trained on a database of 2000 migration barriers, obtained with density functional theory (DFT) in place of interatomic potentials. The method is tested on copper precipitation in thermally aged iron alloys, by means of a hybrid atomistic-object KMC model. For the object part of the model, the stability and mobility properties of copper-vacancy clusters are analyzed by means of independent atomistic KMC simulations, driven by the same neural networks. The cluster diffusion coefficients and mean free paths are found to increase with size, confirming the dominant role of coarsening of medium- and large-sized clusters in the precipitation kinetics. The evolution under thermal aging is in better agreement with experiments with respect to a previous interatomic-potential model, especially concerning the experiment time scales. However, the model underestimates the solubility of copper in iron due to the excessively high solution energy predicted by the chosen DFT method. Nevertheless, this work proves the capability of neural networks to transfer complex *ab initio* physical properties to higher-scale models, and facilitates the extension to systems with increasing chemical complexity, setting the ground for reliable microstructure evolution simulations in a wide range of alloys and applications.

DOI: 10.1103/PhysRevB.95.064112

I. INTRODUCTION

Thanks to the fast-rising capabilities of modern computers, numerical simulations are becoming increasingly important in modeling the structural evolution of solid materials under the most diverse conditions and applications [1]. All macroscopic properties such as hardness or ductility depend on physical phenomena occurring on small spatial and temporal scales that are difficult to analyze experimentally. For this reason, atomistic simulations play a crucial role in unraveling the processes driving the microstructure evolution, in aiding the interpretation of experimental findings, and in building the necessary knowledge to predict the behavior of existing materials, or improve the design of more resilient ones [2,3]. At the microscopic level, the evolution of the system is driven by the migration of crystal defects and impurities, which induce a progressive local chemical redistribution that changes the macroscopic features of the material. Such transformations are either purposely induced to achieve the desired mechanical properties, or occur as a consequence of aging or external events such as irradiation. The latter is responsible for the production of large amounts of defects that accelerate the microstructural changes [4,5]. For instance, the ductility of reactor pressure vessel steels in nuclear power plants is progressively reduced [6,7] during operation by the formation of solute-defect complexes [8–10] and by solute segregation on grain boundaries and dislocations [9,11,12], which occur because of the interaction between neutron-induced defects and impurities or alloying elements.

Among the available modeling techniques (see Becquart and Domain [3] for an exhaustive review), kinetic Monte Carlo (KMC) methods are a common choice for microstructure simulations of metals and alloys. The evolution of rather large atomic structures (beyond the micrometer scale) can be simulated up to real time scales within a reasonable computational time, and with a full spatial description that allows for a direct comparison with experimental characterizations [5,13]. In atomistic KMC (AKMC) simulations, the evolution of the alloy is modeled as a sequence of thermally activated atom jumps, whose transition rates Γ need to be known as accurately as possible. In transition-state theory they are usually expressed as [14]

$$\Gamma = \Gamma_0 \exp\left(\frac{E^{\mathrm{mig}}}{k_{\mathrm{B}}T}\right), \tag{1}$$

*Also at KTH Royal Institute of Technology, Reactor Physics, SE-106 91 Stockholm, Sweden; messina@kth.se

where Γ_0 is an attempt frequency, E^{mig} is the migration energy, and k_B is the Boltzmann constant. Both quantities depend on the migrating chemical species and the local atomic environment (LAE). The reliability of the simulation strictly depends on the accuracy of the parametrization of these quantities. Although they can be calculated with great precision by means of various methods [15–17], such as for instance first-principles calculations, determining all transition rates is inherently unmanageable because of the large number of possible LAE configurations, even in a binary system.

Several methods are normally used to work around this limitation [2,3]. Two approaches may be distinguished amongst them. The most common one is to infer E^{mig} from the energy of the end states [18] (i.e., the equilibrium configurations before and after the jump), which is obtained through a cohesive model based either on pair interactions [19–23], cluster-expansion developments [24–26], or interatomic potentials [27,28]. In this approach, the model is calibrated on the thermodynamic properties of the system, by fixing a target on the equilibrium that the system should evolve to. The second approach consists in targeting directly the prediction of the migration energies, for instance by means of broken-bond models [21,29,30], or advanced regression schemes fitted on a large pool of migration-energy data [31,32]. In the latter case, machine-learning algorithms can be applied to perform an on-the-fly interpolation of a large database of known migration barriers, to provide a best estimate when the LAE of the hopping atom is not included in the database. This was the approach followed by Castin *et al.* [17,31,32] to model copper precipitation in FeCu alloys. Therein, the migration barriers in the KMC model were predicted by artificial neural networks (ANNs) trained over a large data set of migration barriers. The latter was obtained by means of nudged elastic-band (NEB) calculations [33,34] based on a suitable interatomic potential (IAP) [35]. The ANNs led to a considerably more efficient E^{mig} prediction with respect to on-the-fly NEB calculations that would greatly limit the reachable simulation time scales.

Widely employed and applicable equally to both strategies, lattice-free cohesive models like IAPs are developed by fitting mathematical expressions on a broad range of input data, with the aim of replicating the desired properties of the system [35,36]. Two main advantages of IAP-based modeling can be highlighted. First, IAPs ensure a high level of flexibility, since they can be adjusted to reproduce at best some specific target properties that are essential for the intended application of the model. For instance, IAPs can be designed to replicate the stability and mobility of point defects and their clusters in irradiated alloys, based either on first-principles or experimental data, or a combination of both [35–38]. Second, IAPs are computationally cheap and are therefore suitable to perform molecular dynamics (MD) simulations in systems as large as millions of atoms, as well as to produce large databases that can be used as a training pool for advanced regression schemes, e.g., for predicting migration barriers in KMC simulations [17,31]. However, IAPs are limited by their mathematical structure, which usually does not allow the multifold complexity of the alloy to be fully encompassed. Depending on the specific modeling purpose, some compromises are often necessary to improve the accuracy of some properties at the expense of others. More elaborate formalisms than the traditional embedded-atom method (EAM) [39,40] would lead to improvements in this respect, but their fitting procedure is increasingly complex. In addition, fitting an IAP requires large efforts and is not easily transferrable to other systems. IAPs are basically specific to the system they were developed for, and need to be refitted when introducing an additional chemical species, or when choosing to target a different set of properties.

These shortcomings may be addressed by relying more intensively on first-principles calculations. In particular, density functional theory (DFT) provides nowadays the most accurate and physically reliable electronic-structure description of the ground-state properties of materials. The intensive use of DFT calculations for a wide range of materials has unraveled many atomic-scale properties that would not be accessible experimentally, such as for instance the energy landscape of defect migration in alloys [41–45]. However, it is possible to mention at least two main limitations of DFT. First of all, there exist different codes, functionals, and parameter sets, which lead sometimes to discordant predictions, even possibly in disagreement with the experimental evidence. An example is the solubility limit of Cu in Fe: the Perdew-Burke-Erzernhof (PBE) functional [46], as well as the other functionals developed under the generalized-gradient approximation (GGA), considerably underestimate Cu solubility, although PBE still represents the most reliable method to predict most basic properties of iron alloys [29,47]. Second, but most importantly, the extensive application of DFT is still limited by the heavy computational load, which prevents the possibility of performing massive amounts of calculations in systems larger than a thousand atoms. For the latter reason, in spite of the great accuracy of NEB calculations, the calculation of migration energies in KMC simulations has been based so far on restricted DFT data sets [19,21,23]. This limits the amount and the quality of the physical information that is possible to transfer from electronic-structure calculations to mesoscale simulations.

A more intensive and systematic use of DFT data would therefore be beneficial to improve the physical description in a large variety of modeling applications. Neural networks trained over DFT databases have received growing interest, with successful developments (see [48,49], and references therein) and applications to MD simulations of metals and alloys [50,51]. However, to the authors' knowledge, no efforts have been made to achieve a fully DFT-based parametrization of KMC simulations aided by neural networks, most likely due to the heavy computational load required. To this purpose, this work presents a combined DFT-ANN approach to improve the physical reliability of KMC models. ANNs are employed here as on-the-fly, nonlinear regression tools to extract useful hidden information from a pool of DFT-calculated migration barriers. Being trained on a large but manageable set of reference cases, the ANNs allow for the best possible transfer of physical details from DFT to higher-scale methods such as KMC simulations, and for the best possible exploitation of the large DFT database of defect migration barriers here developed (which required approximately 10 million core hours of high-performance computations). As a first test case, it is chosen to investigate the coherent phase of Cu precipitation in thermally aged dilute FeCu alloys, following in most respects the line of

work by Castin *et al.* [31], but replacing the EAM potential with the DFT database. This system is relatively simple to model, because the microstructure evolution is driven by the migration of a single vacancy, with little lattice distortion and in the absence of strong magnetic interactions [47,52]. Hence, the evolution depends exclusively on how the vacancy migration energy varies with respect to the LAE. In this work, ANNs trained over a data set of 2000 migration barriers in varying LAEs are used to parametrize a hybrid atomistic-object KMC model. The ANNs serve as migration-energy predictors for both the atomistic and the object parts of the hybrid model.

Having been thoroughly investigated in the literature [20,29,32,53–58], the FeCu system is well suited for the evaluation of the quality of this DFT-ANN approach, evidencing both its potential benefits and limitations. It can potentially provide an efficient and reliable tool for migration-barrier prediction in KMC simulations as well as in other modeling techniques, while ensuring the best possible transfer of the multifold properties of the alloy, even though the DFT properties can sometimes be affected by uncertainties. In addition, this approach addresses the limitations of system-specific potentials, as most chemical species can be readily and automatically treated by DFT for any complex alloy. Therefore, increasing the chemical complexity of the investigated alloy would be achieved by adding relevant sample cases in the ANN training database, without the need of repeating heavy fitting procedures.

The paper is structured as follows. Section II presents the methodology used to construct the DFT database of migration barriers and to train the neural networks, with particular emphasis on the challenges involved in handling and performing massive sets of DFT calculations. The trained neural networks are then applied in Sec. III to the simulation of thermal aging of FeCu alloys, as well as to the determination of mobility and stability parameters of copper clusters. A discussion of the presented results and a comparison with previous studies follow in Sec. IV.

II. *AB INITIO* BASED NEURAL NETWORK

Artificial neural networks (ANNs) are flexible and powerful tools aimed at learning complex relationships between given input and output variables, for which usually no simple expressions, or interaction laws, can be easily formulated. ANNs are popular instruments in the field of machine learning, and they have been successfully applied to many problems in the most diverse scientific or technical areas [59,60]. In this work, the objective is to develop ANNs able to provide a fast, yet accurate estimate of the activation energy for single vacancy-migration events in KMC simulations, based on a data set of *ab initio* calculations. This is clearly a high-dimensional numerical regression problem, because the migration energy varies as a function of the chemical composition of the local atomic environment (LAE), i.e., the chemical species located in each neighboring site within a given cutoff distance. The input variables for the ANNs are therefore a set of integer numbers that indicate the chemical nature of the neighboring atoms and hence define the LAE univocally. Such a choice leads in principle to a rigid-lattice approach, because the atoms are considered in their invariant spatial positions; however, static relaxations are implicitly treated when constructing the training database of migration barriers with *ab initio* or IAP-based calculations.

The method adopted here is largely inspired from previous works in Fe-Cu and Fe-Cr alloys [17,31,32], which thoroughly demonstrated the feasibility and advantages of using ANNs for vacancy migration-energy estimation. Specific EAM interatomic potentials were therein conveniently used as sources of physical data, because of their simplicity. For instance, there was no practical limitation on the amount of migration energies that could be calculated, and substituting their on-the-fly calculation with the ANN had the only purpose of boosting the AKMC simulation speed by several orders of magnitude. This series of works concluded that optimal ANN predictions could be achieved if a sufficient amount of neighboring sites was included in the LAE, namely approximately 200 lattice sites, which correspond to 1.5 times the EAM potential cutoff distance. This was asserted to guarantee that all effects of chemical interactions, as well as long-range static-strain interactions were adequately transferred from the potential to the KMC model. However, several tens of thousands of migration energies were necessary to properly train the ANN.

Whereas similar numerical requirements could be easily fulfilled with EAM interatomic potentials, addressing them with DFT calculations is evidently a challenging task, seemingly at the very edge of present-day technical possibilities. The approach pursued in the EAM-based works [17,31,32] needs therefore to be adequately adapted in order to limit the huge computational costs inherent to *ab initio* methods, especially with respect to the required computing time and physical memory. To the authors' knowledge, this represents the very first attempt to employ DFT-trained ANNs for the prediction of KMC migration barriers. The present section is dedicated to describing the method followed here to reach a satisfactory compromise between accuracy and complexity, which makes the implementation of DFT-powered neural networks possible.

A. DFT database of vacancy migration energies

The NEB method [33,34] is the most common one to calculate defect migration energies in DFT with high accuracy. However, generating and handling large databases of several thousands of DFT-NEB migration energies undoubtedly raises several challenges. The most obvious and most limiting of them is clearly the computational cost associated with each NEB calculation, which increases quickly with the size of the simulation cell, as well as with the required convergence accuracy on forces and energies. A tempting strategy is therefore to downsize the simulation cell, thus reducing the size of the LAE around the migrating vacancy, and to impose less stringent accuracy requirements. In other words, one could calculate a larger number of less accurate migration energies. Whether the ANN training needs are better addressed with this strategy, however, is to be assessed carefully. Trials and errors are necessary to tell whether the ANN predictions are more accurate with a larger training data set, hence providing more examples of distinct LAE configurations, or with a smaller but more accurate set of data. In this respect, previous experience on ANNs applied to atomistic modeling [17,61] suggests to

avoid simplifications as much as possible. Since the objective here is to transfer to the KMC model the intrinsic quality of the physical representation provided by *ab initio* methods, it seems reasonable to favor accuracy at the expense of the amount of migration barriers included in the ANN training.

A second challenge is represented by the necessity of automatizing the DFT calculations in order to build a large database. This was of no concern with EAM potentials, but it is far less straightforward to handle with DFT. Before the calculation batches are launched, a careful planning of many inner parameters in the DFT method is clearly necessary. The best set is chosen here based on previous experience with NEB calculations in iron alloys [43,45], as well as on testing of a few trial cases. Moreover, since it is practically impossible to inspect the correctness of each calculation individually, all of them are scanned after completion in an automated fashion to search for anomalous behaviors, such as unexpected magnetic moments, tortuous migration paths, or excessively long convergence loops. Although it is very challenging and time consuming to assess the reliability of such anomalous cases, they can be safely removed from the database without affecting the ANN performance, as long as they represent a small fraction of the total amount.

Bearing in mind all the above considerations, it was chosen to aim at building a database of 2000 DFT-NEB migration barriers, which were calculated with the Vienna *ab initio* simulation package (VASP) [62–64]. In order to suit the available computational capabilities, the NEB calculations were performed in $5 \times 5 \times 5$ supercells with a body-centered cubic (bcc) structure, i.e., containing 249 atoms and one vacant site, in fully periodic boundary conditions. The calculations were performed on a plane-wave basis, using the standard projector-augmented wave (PAW) pseudopotentials [65,66] available in the VASP library. The Perdew-Burke-Erzernhof (PBE) parametrization [46] of the generalized-gradient approximation was employed to sample the exchange-correlation function. All calculations were spin polarized, and the spin interpolation of the correlation potential was achieved by means of the Vosko-Wilk-Nusair algorithm [67]. The Brillouin zone was sampled with the Monkhorst-Pack scheme. The plane-wave cutoff was set to 300 eV, and a k-point mesh of $3 \times 3 \times 3$ was chosen in accordance with the convergence tests of a previous work [68]. The resulting equilibrium lattice parameter is $a_0 = 2.831$ Å. For each of the 2000 transitions, the end-state configurations were first relaxed allowing for ionic relaxations, but restraining the cell volume. Afterwards, the migration barriers were calculated with the NEB method using three intermediate images and the climbing-image algorithm [33,34]. Some preliminary tests performed on a few problematic cases with complex EAM energy paths confirmed the suitability of this choice. In order to boost the computational efficiency, each NEB calculation was performed first with a reduced amount of k points ($2 \times 2 \times 2$), and the energy of the found saddle point was then recalculated with the full k-point mesh ($3 \times 3 \times 3$) without allowing for ionic relaxation. This accelerated procedure was tested on a few cases and proved not to be detrimental for the calculation accuracy. It is worth mentioning that in some cases the convergence of the end-state relaxation was greatly improved by providing an initial magnetic moment that is only slightly enhanced (2.3 Bohr magnetons) with respect to the experimental value [69]. To quantify the actual computational cost, one NEB calculation with 249 atoms required approximately 5000 core hours on the high-performance computers used for this work, hence the total cost for the whole database of 2000 migration barriers amounted to approximately 10 million core hours.

In addition, ANN training experiments based on the EAM potential [35] were performed as a complementary benchmark of the quality of this approach. In brief, the EAM potential was used to generate several training databases of vacancy migration energies, in simulation cells mimicking the parameters of the 249-atom DFT supercell, and to investigate the sensitivity of the resulting ANN performance with respect to the volume of the training database (from 500 to 10 000 cases), as well as to the accuracy of each EAM barrier calculation (in terms of residual saddle-point forces). The results of this parallel study, not detailed here for the sake of conciseness, supported the adequacy of the parameters chosen to build the DFT database, especially concerning the size of the simulation cell (249 atoms) and that of the training database (2000 migration barriers).

B. Selection of relevant atomic configurations

As already mentioned, the training database for the neural networks consists of 2000 vacancy migration energies, with varying local atomic configurations. In practice, each case differs from the other for the amount and distribution of Cu atoms in the simulation cell. The neural networks are meant to drive AKMC simulations of thermal-annealing experiments in FeCu alloys, focusing in particular on the early stages of Cu precipitation. It is therefore crucial that the ensemble of cases in the database provides an exhaustive description of the configurations that might be encountered during the simulation. Based on the past experience in the modeling of FeCu alloys [31,32], there are mainly three types of local configurations to be distinguished, as is described in Fig. 1:

(i) Type-I configurations are representative of the very early stages of the simulation. The studied alloy is still a random solid solution of Fe and Cu atoms, in a bcc structure, with a small Cu content (<5%). Mass transport led by vacancy diffusion produces a rearrangement of Cu atoms, and small clusters are progressively seeded. The latter, however, are likely to dissolve unless they grow above a critical size, here estimated at about 10 to 15 Cu atoms. Consequently, the LAE around the migration vacancy is, at this stage, a random solid solution, with the occasional occurrence of small clusters.

(ii) Type-II configurations represent cases of vacancy diffusion in the vicinity of small, stable Cu clusters, i.e., above the critical size. Because of the strong demixing tendency, no Fe atoms are expected to be found inside Cu aggregates. As was observed in previous works [29,31], the expected driving force at this stage is the diffusivity of these small Cu clusters, which are mobile because of successive hops of the vacancy at their surface. This diffusivity is expected here to be replicated spontaneously by the DFT-based neural network, as a balance of all possible vacancy jumps.

(iii) Type-III configurations are expected at more advanced stages, when large Cu clusters (>1000 atoms) are formed.

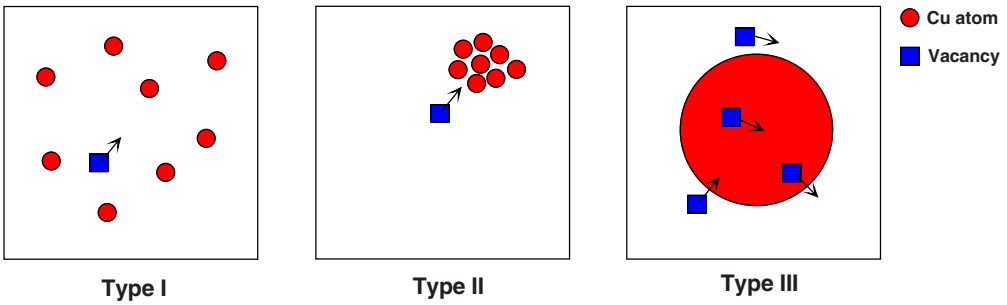

FIG. 1. Types of local atomic environment around a migrating vacancy (blue squares) that are expected to be encountered during the simulation of thermal-aging experiments: (I) random distribution of Cu atoms (red circles) up to 5 at. % in an Fe matrix; (II) vacancy jump in the vicinity of small Cu clusters; and (III) vacancy jump inside, next to, or across large Cu clusters. Because of supercell size limitations, the DFT database does not include type-III configurations, and the cluster size in type-II arrangements is limited to 80 atoms.

Here the vacancy diffuses in the vicinity of a smooth Fe-Cu interface. Such large clusters are still expected to be mobile to some extent, after a much longer sequence of vacancy migration events at their surface. However, no cases of this kind could be included in the DFT database due to the supercell size limitations.

Given the limited size of the DFT supercell (250 atoms), necessary to limit the computational cost of DFT calculations and fit the resources allocated for this work, it is clear that type-III configurations as well as intermediated configurations between types II and III cannot be included in the DFT database. A 250-atom supercell is insufficient to fit a realistic interface between the Cu cluster and the Fe matrix; moreover, since the aim is to simulate coherent precipitation (i.e., in a full bcc structure), the total fraction of Cu atoms in the supercell cannot exceed 50%, at the very most. For these reasons, type-III configurations were unavoidably excluded from the DFT database, and even type-II configurations were limited to Cu clusters up to 80 atoms. The 2000 cases for the DFT database were therefore selected in the following way:

(1) 1000 configurations of type I were chosen at random. An additional set of 1000 configurations of type II were extracted from previous AKMC simulations performed with the EAM potential [35]. This aided selection of Cu-cluster "snapshots" is deemed to be more reliable than a completely random selection, because it is based on an actual physical model.

(2) In order to maximize the variability and avoid the accidental repetition of similar cases, the diversity of the LAEs in the database was carefully assessed. This was achieved by considering as well all possible symmetry transformations.

(3) Again in the aim of constructing a heterogeneous database, the selection was conducted by maximizing the diversity of the migration-energy values, as well as that of the equilibrium-energy difference between initial and final state. Since such quantities are obviously unknown beforehand (it is, after all, the actual purpose of the ANN), the EAM potential was used to obtain these values and help making a better educated guess.

In summary, the procedure described above was aimed at selecting the best possible database of reference cases, given the box-size limitation. This set of cases guarantees that the very early stages of Cu precipitation are adequately included in the ANN training database. Therefore, once trained, the ANN performance during the later stages, i.e., when larger clusters are formed, is in principle not fully guaranteed, given the absence of relevant cases in the training database. Appropriate testing based on the EAM potential seems to confirm a small DFT-ANN prediction error on type-III barriers; nevertheless, the actual reliability of the simulation in the late precipitation stages is carefully assessed in Secs. III and IV.

C. ANN architecture and training

The ANNs to be trained on the DFT database were designed in order to maximize prediction accuracy and calculation efficiency. Since the topic has already been thoroughly treated in previous publications (the interested reader is referred in particular to the work by Castin and Malerba [17]), providing a detailed description of the ANN design and training methodology goes beyond the scope of the present paper. Here the essential aspects are summarized:

(i) The database is split in two separate subsets: the training set (1300 cases) is used to fit the ANNs, whereas the reference set (700 cases) serves as benchmark to measure the accuracy of prediction for "never-seen" cases.

(ii) The symmetries of the bcc structure are fully exploited. Each NEB calculation provides two examples of migration events (the forward and backward jump), and the application of the six possible symmetry operations leads to a total number of 12 LAE configurations that are used as input for the ANNs. In practical terms, the actual size of the training set is thus 15 600 entries, and that of the reference set is 8400.

(iii) Adequate trials led to the conclusion that the ANN accuracy optimum is achieved when the LAE extends up to the fifth nearest neighbors (5nn) of both the vacancy and the jumping atom. The total number of ANN input variables is therefore 76, corresponding to the chemical species located in each of the LAE sites. The chemical species of the hopping atom is not included as input because, based on past experience, it was chosen to design two separate ANNs for the migration of Fe atoms (first ANN) and Cu atoms (second ANN).

(iv) The optimal ANN architecture can be customized depending on the complexity of the problem. It may consist of

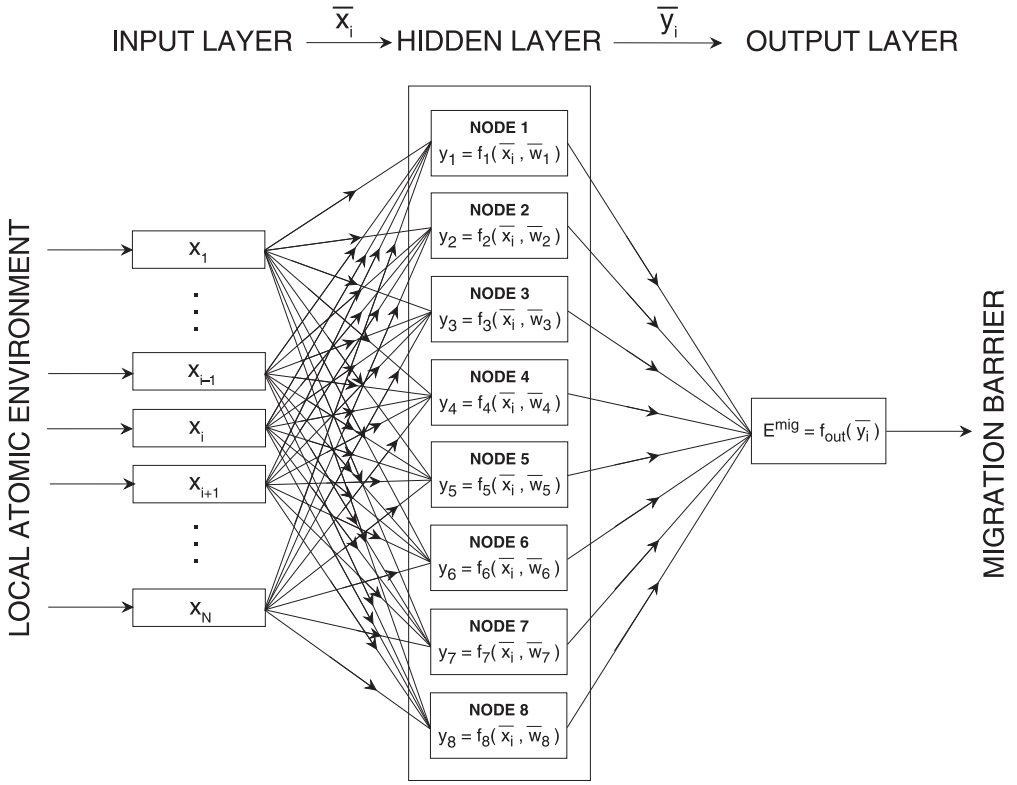

FIG. 2. Structure of the artificial neural networks for the prediction of the migration barrier corresponding to a given local atomic environment. The latter is described by the occupancy of the 76 sites within a 5nn distance from the initial and final position of the jumping atom (input $\bar{x}_i$). Using the training set of migration barriers, the parameters w_j are fitted through a least-square method procedure to minimize the predicting error on the validation data set. A more detailed explanation of the same architecture is provided in another publication [70].

one or several hidden layers, and a freely choosable number of nodes [60]. Analogously to previous works [17,31], it is chosen here to rely on the lightest possible structure that ensures the best reasonable predictions, consisting of one hidden layer and eight nodes (Fig. 2). The amount of adjusting parameters, denoted as w_j in the figure, is 625.

(v) Finally, given the network structure and the training database, the training consists in determining the best suited numerical value for the inner parameters. It is achieved by minimizing with the Levenberg-Marquardt method the mean-square discrepancy between the DFT validation energy barriers and the corresponding ANN predictions.

After training the ANNs on the DFT database, the predictive performance is shown in Fig. 3, where the DFT barriers of the reference set are compared to the corresponding ANN predictions. The average prediction error is 23.5 meV, which confirms the quality of this approach. However, there exist a few outlying cases. These outliers correspond to configurations where the DFT energy difference between the end states is very large (up to 1.8 eV), and the NEB simulation yields a smooth barrierless transition between the two states. A closer look reveals that they correspond to very unlikely events, where an iron atom is attempting to move towards or inside a medium-sized Cu cluster. Such a transition is clearly unfavorable from an energetic standpoint, because of the demixing tendency of the FeCu alloy. These rare, extreme cases are not well reproduced by the ANN because they are poorly sampled in the training data set. At any rate, they can be safely neglected and removed from the database, since they are surely irrelevant for the KMC simulation, and they represent just a small fraction of the total amount of cases (0.2%).

III. KINETIC MONTE CARLO SIMULATIONS

A. Hybrid AKMC-OKMC model

The ANNs presented in the previous section are applied here to simulations of thermal aging in FeCu alloys. This is achieved in the framework of a hybrid AKMC-OKMC model that is in most respects analogous to that of the previous EAM-ANN work [31]. The system is represented by a periodic bcc crystal, in a $200 \times 200 \times 200\ a_0^3$ supercell, containing an initially random mix of iron and copper atoms on a rigid lattice and a vacant site. The evolution of the system proceeds through a series of vacancy jumps, which are randomly selected based on the LAE-dependent transition rates as in Eq. (1). The simulation time is then increased with the traditional residence-time algorithm [71]. The migration barriers of such rates are predicted "on-the-fly" by the neural networks. The attempt frequencies Γ_0 are also in principle LAE dependent: for instance, the attempt frequency for the migration of an iron atom is about 2.5 times larger than that of a copper atom [72]. However, since attempt-frequency calculations are extremely demanding in terms of computational cost, it was not chosen at this stage to design additional neural networks for the prediction of Γ_0. For this reason, it is here assumed

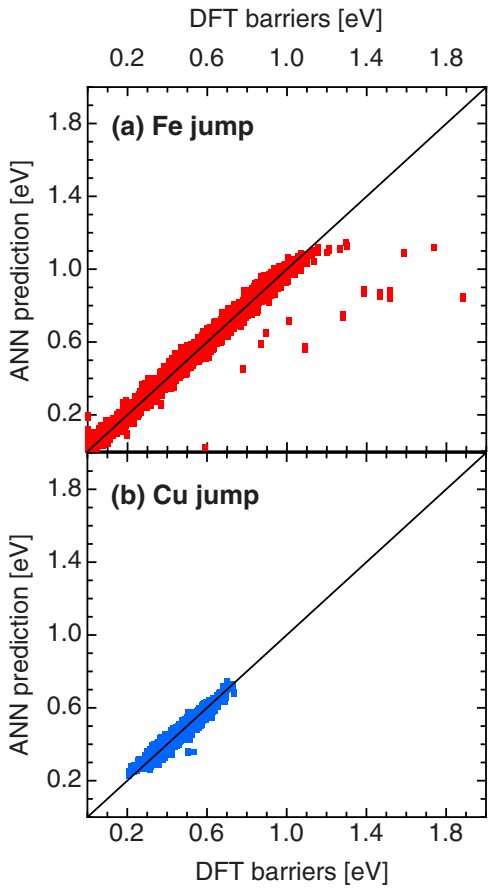

FIG. 3. Neural-network prediction of DFT migration barriers from the validation set for (a) Fe-atom and (b) Cu-atom jumps. The average prediction error is 23.5 meV, with a Pearson's correlation coefficient $R^2 = 0.999$.

in first approximation that $\Gamma_0 = 6$ THz for any transition, in analogy to previous studies [19,31].

Given the lower vacancy formation energy in bcc copper (about 0.9 eV [29]) than in Fe (2.18 eV [45]), the vacancy is most often trapped inside Cu clusters. For the sake of computational efficiency, the KMC simulation is accelerated by introducing a coarse-grain approximation, i.e., by treating clusters above a certain size as new entities with their proper behavior (i.e., "objects" in KMC jargon). In this hybrid approach, the AKMC algorithm applies as long as the vacancy is located outside any Cu cluster, or next to small ones. This allows for the detailed reproduction of atomistic mechanisms such as the vacancy drag of single Cu atoms [45]. Conversely, when the vacancy reaches a Cu cluster above a user-defined size threshold, the cluster is "activated," i.e., it becomes a unique entity that can migrate, dissociate, or react with other entities. The evolution of an activated cluster is simulated with an OKMC algorithm until the vacancy is emitted. The size threshold here is set to 15 atoms, corresponding to the very stable configuration of one central atom surrounded by fully occupied 1nn and 2nn shells. Once activated, the cluster immediately absorbs all Cu atoms located within the 2nn distance from its surface. Three events are then allowed:

(1) Vacancy emission, possibly combined with the emission of some Cu atoms.

(2) Migration of the cluster by a 1nn distance $\Delta = \sqrt{3}a_0/2$, where a_0 is the lattice parameter, and subsequent absorption of all Cu atoms within the interaction range in the new position.

(3) Coalescence of clusters with overlapping interaction ranges.

The maximum Cu-cluster size is set to 6000 atoms in order to remain within the limits of coherent precipitation (corresponding approximately to a precipitate radius of 2.5 nm) [31,73]. The cluster stability and mobility parameters (i.e., dissociation and migration frequencies) are obtained with independent AKMC simulations based on the same DFT-ANN model, as is detailed in Sec. III B.

For the sake of comparison with thermal-aging experiments, the simulation time t_{MC} must be rescaled in order to match the thermal-equilibrium vacancy concentration:

$$t_{\mathrm{real}} = t_{\mathrm{MC}} \frac{c_{\mathrm{v}}^{\mathrm{MC}}}{c_{\mathrm{v}}^{\mathrm{eq}}}. \tag{2}$$

As highlighted by previous works [29,31], the vacancy concentration in the simulation $c_{\mathrm{v}}^{\mathrm{MC}}$ must be corrected with the fraction of time f_{v} spent by the vacancy far from Cu atoms:

$$c_{\mathrm{v}}^{\mathrm{MC}} = \frac{f_{\mathrm{v}}}{N_{\mathrm{at}} c_{\mathrm{Fe}}}, \tag{3}$$

where N_{at} is the number of atoms in the simulation cell, and c_{Fe} is the concentration of Fe atoms. Thanks to this correction, the difference in vacancy formation energy between an Fe-rich environment and a Cu-rich one is correctly taken into account. However, since f_{v} is measured directly during the KMC simulations, the vacancy formation energies on both the Fe-rich and Cu-rich sides are intrinsic outcomes of the DFT-ANN cohesive model, rather than explicit input parameters. On the other hand, the vacancy concentration in thermal equilibrium in pure Fe is an input parameter for time rescaling, and is expressed as

$$c_{\mathrm{v}}^{\mathrm{eq}} = k \exp\left(-\frac{H_{\mathrm{v}}^{\mathrm{f}}}{k_{\mathrm{B}} T}\right) \exp\left(\frac{S_{\mathrm{v}}^{\mathrm{f}}}{k_{\mathrm{B}}}\right). \tag{4}$$

The values adopted here for the pure-iron vacancy formation enthalpy $H_{\mathrm{v}}^{\mathrm{f}} = 2.18$ eV [45] and entropy $S_{\mathrm{v}}^{\mathrm{f}} = 4.1\, k_{\mathrm{B}}$ [74] are taken from previous DFT calculations. In Eq. (4) factor k accounts for various uncertainties, such as the presence of other impurities and the simplifications regarding the attempt frequencies. In the previous EAM-ANN work [31], this factor was treated as a fitting parameter to the experimental results; however, it should be ideally independent of temperature and composition and as close as possible to unity. It can therefore be taken as a quality benchmark for the KMC physical model.

B. Properties of Cu clusters

The OKMC part of the algorithm is parametrized by means of independent AKMC simulations aimed at obtaining the cluster migration and vacancy-emission frequencies as functions of size and temperature, as well as investigating the possible emission patterns. This is achieved by applying a consolidated procedure fully explained in previous works [31,56,75] and here briefly summarized. A given cluster vCu_n is introduced in an otherwise pure-Fe simulation cell

$(50 \times 50 \times 50\, a_0^3)$ and let evolve under the traditional AKMC algorithm. The simulation is then interrupted upon vacancy emission from the cluster. The transition rates are given by the trained DFT-ANN network described in Sec. II. This procedure is repeated 10^2 to 10^3 times, depending on temperature and cluster size, in order to gather sufficient statistics to calculate the average lifetime before emission τ_n and the mean square displacement $|\vec{R}_n|^2$. The emission frequency is given by the inverse of the lifetime:

$$\Gamma_n^{\mathrm{em}} = \frac{1}{\tau_n}, \tag{5}$$

whereas the cluster diffusion coefficient D_n is obtained from the mean square displacement, according to classical diffusion theory [14]

$$D_n = \frac{|\vec{R}_n|^2}{6\tau_n}. \tag{6}$$

From the diffusion coefficient, the cluster migration frequency is calculated as

$$\Gamma_n^{\mathrm{mig}} = \frac{6D_n}{\Delta^2}, \tag{7}$$

where Δ is the 1nn jump distance. In Eq. (7) correlations are neglected, which is acceptable as long as a large number of trajectories is simulated and averaged.

The simulations are performed for selected cluster sizes ($15 < n < 6000$) at selected temperatures ($500 < T < 4000$ K). For each cluster size, a continuous variation in temperature is obtained by performing a linear fitting in the Arrhenius domain (see for instance Fig. 4), which yields the prefactors $\Gamma_{0,n}$ and the activation energies E_n for migration and vacancy emission:

$$\Gamma_n^{\mathrm{mig}}(T) = \Gamma_{0,n}^{\mathrm{mig}} \exp\left(-\frac{E_n^{\mathrm{mig}}}{k_{\mathrm{B}}T}\right), \tag{8}$$

$$\Gamma_n^{\mathrm{em}}(T) = \Gamma_{0,n}^{\mathrm{em}} \exp\left(-\frac{E_n^{\mathrm{em}}}{k_{\mathrm{B}}T}\right). \tag{9}$$

Finally, in order to obtain a smooth variation of Γ_n^{mig} and Γ_n^{em} as functions of cluster size at specific simulation temperatures T^*, the following fitting functions are used:

$$\Gamma_{n,T^*}^{\mathrm{mig}} = \begin{cases} \mathrm{A}(\ln n)^{\mathrm{B}} & \text{for } n \leqslant 450, \\ \mathrm{C}\exp(\mathrm{D}\ln n) & \text{for } n > 450, \end{cases} \tag{10}$$

$$\Gamma_{n,T^*}^{\mathrm{em}} = \begin{cases} \exp[\mathrm{E}(\ln n)^{\mathrm{F}}] & \text{for } n \leqslant 450, \\ \exp[\mathrm{G}\ln(\ln n) + \mathrm{H}] & \text{for } n > 450. \end{cases} \tag{11}$$

The units for the temperature-dependent parameters (A through H) are defined so that the migration frequencies are expressed in s^{-1}. Their numerical values for the chosen simulation temperatures are reported in Table I.

The diffusion coefficients and lifetime of a few selected cluster sizes are shown in Fig. 4, where they are compared to the calculations by the EAM-ANN method [31] (open symbols). The continuous lines represent the linear fitting for each cluster size, whose results in terms of activation energies and prefactors are presented in Fig. 5. In the same figure, the binding energy between the vacancy and the copper cluster (green line) is obtained in first approximation as $E^{\mathrm{b}} = E^{\mathrm{em}} - E^{\mathrm{mig}}$. As expected, this binding energy increases with cluster size before reaching a plateau. In the limit of very large clusters, the binding value at the plateau can be interpreted as the segregation energy of a vacancy on a bcc Fe/bcc Cu interface, which is here estimated in about 0.9 eV.

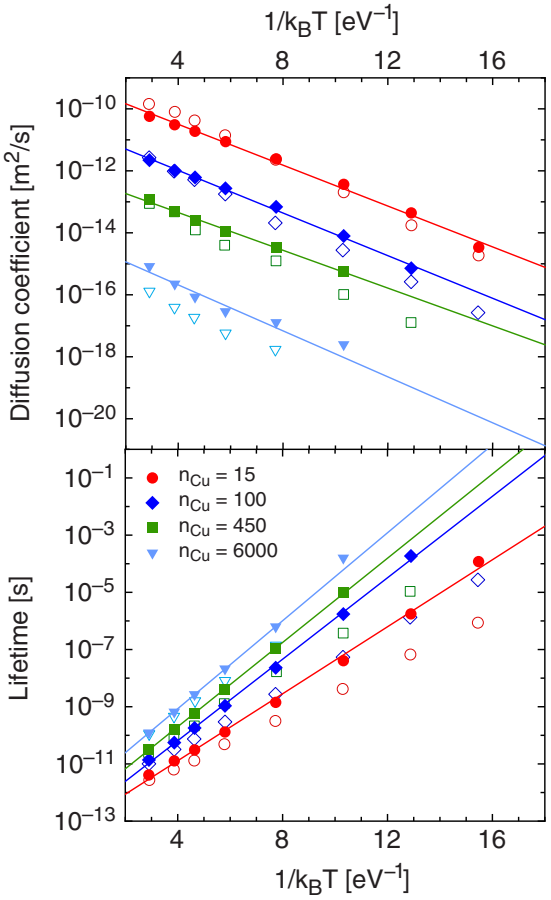

FIG. 4. Average diffusion coefficients (above) and average lifetime before vacancy emission (below) of copper clusters containing a vacancy, as obtained by means of AKMC simulations based on the *ab initio* trained neural networks. The open symbols represent the results obtained with the previous EAM-ANN approach [31].

The vacancy-copper complexes are found in this work to be considerably more stable and slightly more mobile with respect to the corresponding EAM-ANN predictions, as they are characterized by larger dissociation and lower

TABLE I. Fitting parameters for the vacancy-emission frequency (Γ_n^{mig}) and migration frequency (Γ_n^{mig}) of Cu clusters in the hybrid KMC model [Eqs. (10) and (11)].

Γ_n^{diss} (1/s)	773 K	823 K	873 K	973 K
A	6.89×10^{8}	1.74×10^{9}	3.95×10^{9}	1.58×10^{10}
B	−6.980	−7.130	−7.262	−7.487
C	2.57×10^{10}	3.44×10^{10}	4.45×10^{10}	6.88×10^{10}
D	−2.683	−2.628	−2.579	2.496
Γ_n^{mig} (1/s)				
E	32.935	27.879	25.946	24.808
F	−1.174	−0.905	−0.744	−0.560
G	−7.200	−6.929	−6.689	−6.283
H	16.862	17.899	18.820	20.372

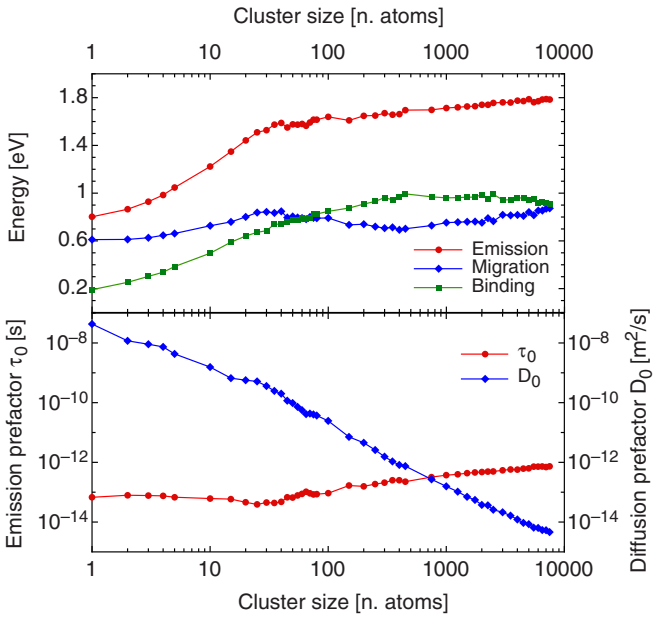

FIG. 5. Migration, dissociation, and binding energy (above) and emission and diffusion prefactors (below) for copper clusters of increasing size, obtained by Arrhenius fitting in the temperature range 750–4000 K. The AKMC binding energy is obtained in first approximation as the difference between the emission and the migration energy.

migration energies. More importantly, the mean free paths (MFPs) $\vec{R}_n$ are significantly longer, reaching up to several lattice units, as is shown in Fig. 6. This is mainly due to the greater stability (intended as the likelihood of the vacancy to remain inside the Cu cluster, rather than the stability of the cluster as a whole). Hence, replacing the interatomic potential with DFT leads to a notably longer-ranged migration of Cu clusters. In addition, the MFP increases with cluster size up to approximately 100 atoms, although this effect disappears above 1125 K. This suggests that large clusters can actually cover longer distances with respect to small ones, even though with a lower diffusion coefficient. It is therefore reasonable to expect that the coalescence of medium-sized clusters, which was previously found to be one of the main features driving Cu precipitation [31], should play here an even more important role.

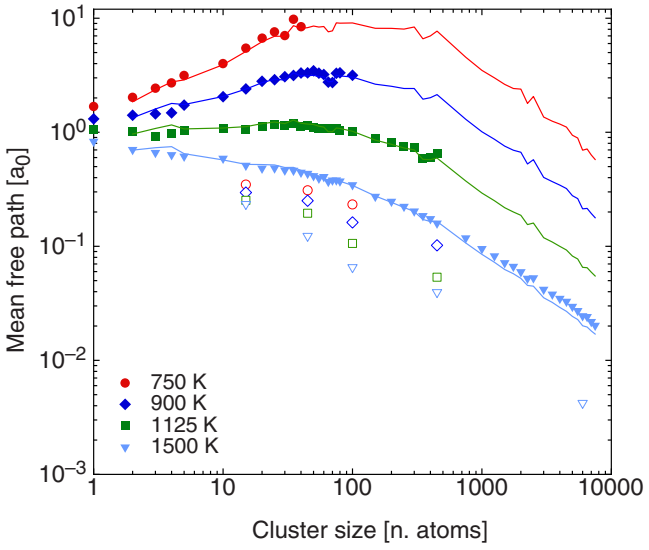

FIG. 6. Average mean free path (in lattice-parameter units) of copper clusters of varying size, as obtained with the DFT-ANN approach (full symbols) and compared to the EAM-ANN work [31] (open symbols). The continuous lines are calculated from the Arrhenius interpolation of diffusion coefficients and mean lifetime, corresponding to the continuous lines of Fig. 4.

It should be noticed that the diffusion coefficients shown in Fig. 4 represent the mobility of the cluster *when the latter contains a vacancy*, which corresponds to the property needed to parametrize the OKMC part of the simulation. The real diffusion coefficient depends as well on the probability of having the vacancy inside the cluster, which is related to the vacancy-cluster binding energy. Since this binding energy increases with size (Fig. 5), it is possible to expect that the diffusion coefficient might also increase with size, in agreement with the findings by Soisson and Fu [29] and as opposed to the data shown in Fig. 4. This issue is discussed in more detail in Sec. IV A.

The analysis of the vacancy emission patterns in each simulation reveals another novel feature with respect to the EAM-ANN work. Therein, the emission of the vacancy occurred sporadically as a vacancy-copper pair, but with such a low frequency that it was possible to neglect this event in the hybrid KMC model. Conversely, the DFT-trained ANN gives here rise to a more evident tendency, namely a more systematic emission or "loss" of several copper atoms before the emission of the vacancy. The recorded average number of emitted atoms $\bar{x}^{\mathrm{em}}_{\mathrm{Cu}} = 1.25$ is independent of cluster size and temperature up to 1125 K, as is shown in Fig. 7. Above this temperature, the average loss of Cu atoms drastically diminishes because of the damping of the vacancy-copper interactions ($\propto \exp[E/k_{\mathrm{B}}T]$), as is discussed in Sec. IV. This phenomenon is included in the present hybrid KMC

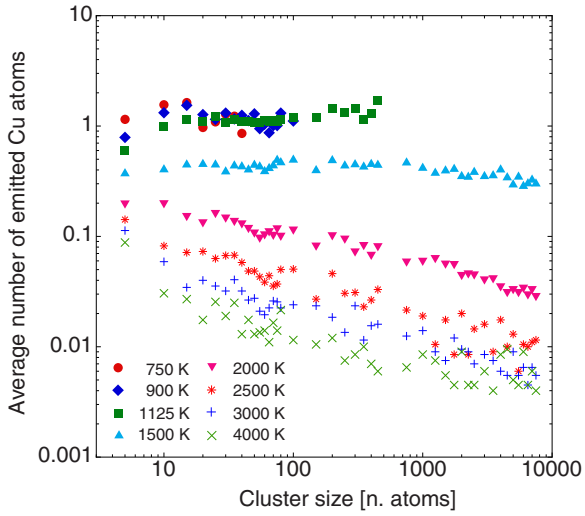

FIG. 7. Average number of Cu atoms lost by the copper cluster before vacancy emission, as a function of cluster size and temperature.

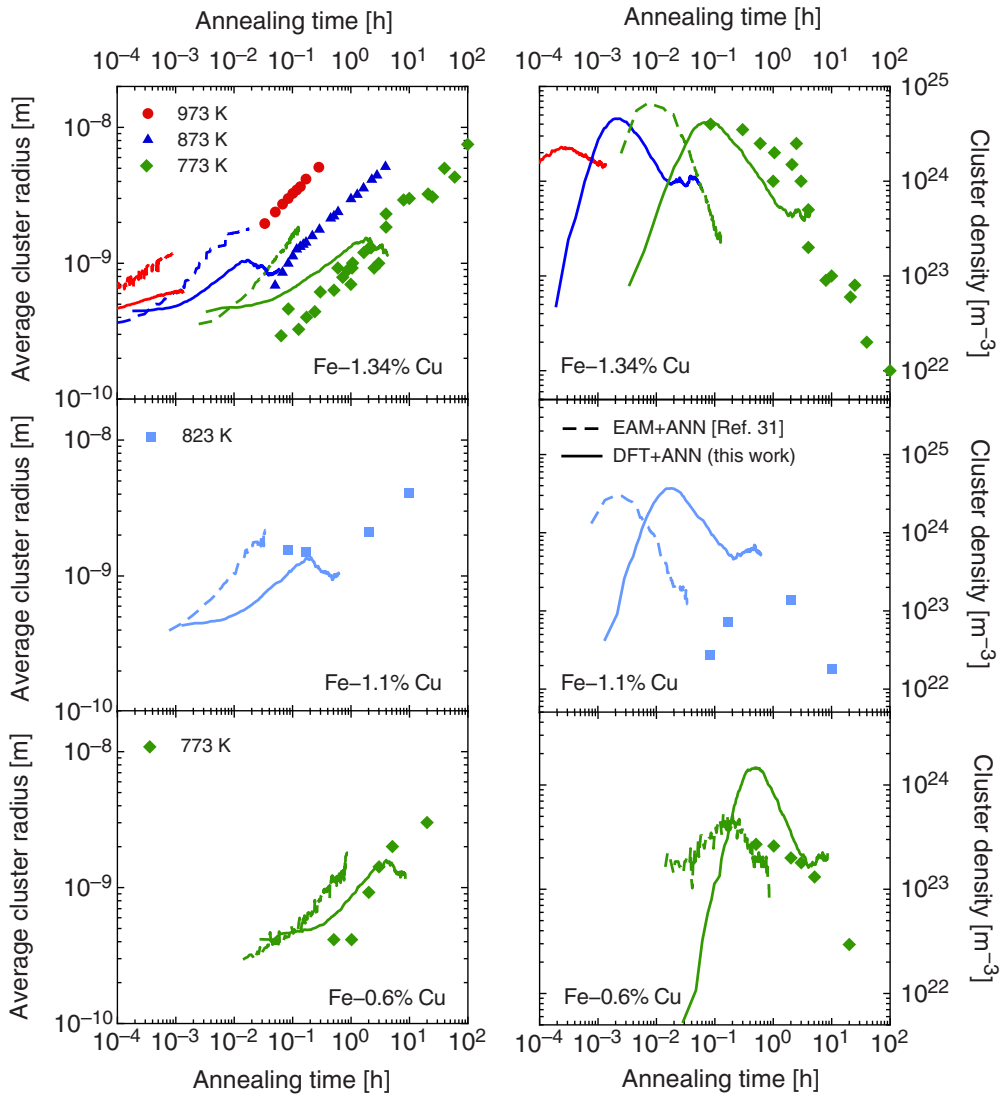

FIG. 8. Comparison with experimental data [20,76–80] of the microstructure evolution of thermally aged FeCu alloys, obtained by means of the hybrid KMC model (solid line) based on the DFT-ANN prediction of transition rates and copper-cluster properties. The dashed lines represent the evolutions yielded by the previous EAM-ANN work [31], adjusted by setting $k = 1$ and introducing a formation-entropy term in the equilibrium vacancy concentration [Eq. (4)]. The reliability of the first two experimental points in the Fe-1.1%Cu alloy [78] is questionable because of a clear contradiction with the evolution of the other alloys [31].

simulations by associating the vacancy-emission event with the emission of an integer number x of Cu atoms, where x is randomly chosen according to a probability distribution function with average $\bar{x}^{\mathrm{em}}_{\mathrm{Cu}}$.

C. Thermal-aging simulations

The hybrid KMC model is applied to simulate the thermal-aging evolution of three different FeCu alloys containing respectively 1.34, 1.1, and 0.6 at. % Cu. The average cluster size and number density are compared with small-angle neutron scattering and atom-probe tomography measurements [20,76–80]. The cluster analysis is performed by considering only clusters larger than 25 atoms, for the sake of consistency with the minimum size detectable with the aforementioned experimental techniques (≈0.5 nm). The choice of the size cutoff has anyway little effect on the results.

The evolution of the cluster average size and number density is shown in Fig. 8, and the main results are summarized in Table II. More simulations (not shown) were performed at varying cell sizes, as well as by rising the size threshold for treating clusters as objects to 30 Cu atoms (as opposed to 15 atoms). The box-size effect was found to be negligible on the aging evolution, whereas extending the AKMC algorithm to larger clusters led to a slight anticipation of the precipitation process, although in all cases the mismatch with the evolutions shown in Fig. 8 vanishes in the later precipitation stage, when large clusters appear.

The time rescaling to the equilibrium vacancy concentration was done by imposing $k = 1$ [Eq. (4)]. In Fig. 8 the results of this work (continuous lines) are compared to those obtained with the EAM-trained ANN (dashed lines) [31]. The latter have been readjusted by setting $k = 1$, and by adding the formation-entropy term ($\exp[S^{\mathrm{f}}_{\mathrm{v}}/k_{\mathrm{B}}]$) to the equilibrium

TABLE II. Summary of the thermal-aging simulation results, showing the number of Cu clusters (N_{cl}) at the density peak and at the end of the simulation, the average cluster radius $\bar{r}_{cl}$ at the size peak and at the end, and the time spent by the vacancy in a pure-iron environment (f_v). The minimum value of f_v corresponds to a complete phase separation [29].

Cu content (at. %)	Temperature (K)	AKMC events (10^{10} events)	N_{cl} (at peak)	N_{cl} (at end)	$\bar{r}_{cl}$ (at peak) (nm)	$\bar{r}_{cl}$ (at end) (nm)	f_v (at end)	f_v^{min}
0.6	773	1.71	573	68	1.59	1.19	2.14×10^{-5}	7.48×10^{-7}
1.1	823	1.70	1309	167	1.37	1.05	1.46×10^{-5}	1.30×10^{-6}
1.34	773	1.64	1559	131	1.54	1.15	2.35×10^{-6}	3.32×10^{-7}
1.34	873	1.68	1679	291	1.06	0.91	2.97×10^{-5}	3.00×10^{-6}
1.34	973	1.75	1088	721	0.63	0.61	1.47×10^{-3}	1.73×10^{-5}

vacancy concentration, in order to make the two simulation sets fully comparable. Figure 8 shows that the DFT-based parametrization yields a substantial delay in the precipitation with respect to the EAM-based model, in much closer agreement with experiments and without the need for any adjusting factor.

The evolution of the Fe-1.34%Cu alloy seems to be well reproduced, especially at 773 K. At higher temperatures (873 and 973 K), the simulation has not reached the experimental time scale because of the long computational time required, but the size evolution trend seems to be compatible with the measured values. At these temperatures, it is not possible to state with certainty whether a time scale adjustment ($k \neq 1$) is needed or not. The cluster-size evolution in the Fe-1.1%Cu alloy is seemingly well reproduced, but the prediction of the number density is in clear disagreement, as was the case for the simulations based on the EAM-ANN method [31]. Considering the incompatibility of the number-density evolution with respect to the other alloys (the number density at 1.1% Cu is expected to be somewhat larger than that at 0.6% Cu), this consistent mismatch suggests that the data points in this experiment [78] may be affected by mistakes or large uncertainties. Finally, the evolution of the Fe-0.6%Cu alloy matches the experimental cluster size, but not the number density: namely, the KMC simulations lead to a large excess of Cu precipitates, or in other words to an underestimation of the Cu solubility in Fe.

Finally, Table II shows that the time fraction spent by the vacancy in a pure-iron environment (f_v) has yet not reached the minimum value corresponding to a complete phase separation (f_v^{min}) that is calculated following the method by Soisson and Fu [29]. Although the precipitation process is not complete, especially at higher temperatures where the KMC time proceeds by smaller steps, the three phases of precipitation can be clearly recognized: nucleation (increase of density and size), growth (stable density while the size continues to increase), and coarsening (size increase with density decrease). However, it is possible to notice that the coarsening phase comes to an unexpected stop, as is shown by the sudden size decrease and density stabilization. The latter occurs when the average size has reached 1000 to 1500 atoms (1.4 to 1.6 nm) in all cases. Since the simulation cell is sufficiently large to have a statistically significant amount of clusters, this unexpected behavior raises an issue on the validity of the model in the late stage of the coarsening phase.

IV. DISCUSSION

A. Diffusivity of copper clusters

Replacing the EAM interatomic potential [31] with DFT was shown to lead to vCu_n clusters that are more stable and can cover longer distances in the lattice. The stability is strongly enhanced by the low vacancy formation energy in bcc copper that arises from the DFT-based parametrization (about 0.9 eV [29]), compared to that in bcc iron (2.18 eV [45]). Furthermore, the loss of isolated Cu atoms can be explained in terms of a competition between the vacancy-cluster binding energy and the strong kinetic coupling of single Cu atoms with vacancies [72]. In dilute iron alloys, many chemical species diffuse via a vacancy-drag mechanism below a solute-dependent temperature threshold. The limit temperature for copper solutes (approximately 1100 K) [72] is very close to the temperature above which Cu clusters cease to emit single Cu atoms (Fig. 7). In addition, it corresponds as well to the temperature above which the long-ranged cluster diffusion is damped (Fig. 6). This suggests that the strong vacancy-copper correlations are supposedly in competition with the cluster stability, although the actual coupling tendency in a more Cu-rich environment is yet unknown and might differ from that in dilute alloys.

The cluster mobility can be compared to the work of Soisson and Fu [29], where it was investigated by means of AKMC simulations based on a pair-interaction broken-bond model. That model was fitted on a set of *ab initio* data, including few jump frequencies. The authors found that the diffusion coefficient increases with cluster size up to approximately 150 atoms. This was explained by the greater vacancy concentration near the cluster surface with respect to the bulk, under the assumption that cluster migration is driven by vacancy jumps occurring next to the surface.

Figure 9 shows the comparison between the diffusion coefficients calculated in this work with those by Soisson and Fu, as functions of the cluster size. Specifically, Fig. 9(a) reports the diffusion coefficients as obtained with the AKMC procedure described in Sec. III B, i.e., by recording displacements and diffusion time only while the vacancy is inside the cluster, and by applying Eq. (6) without rescaling the time to the equilibrium vacancy concentration [Eq. (2)]. It is possible to notice that, under such assumptions, the diffusion coefficients do not increase with size, as opposed to the findings by Soisson and Fu [29]. However, the increasing mobility with size evidenced by the aforementioned study matches the increase

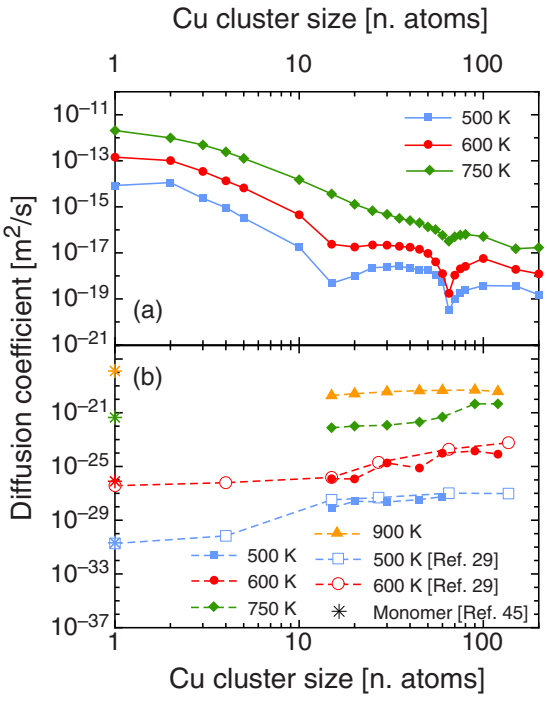

FIG. 9. Diffusion coefficients of vCu_n clusters as functions of cluster size n, from Eq. (6), compared to the KMC simulations by Soisson *et al.* based on a broken-bond pair-interaction model [29]. (a) Simulations stopped upon vacancy emission, with no time rescaling. (b) Simulations performed by allowing the vacancy to explore pure-Fe environments, and applying the time rescaling according to Eq. (2). The star symbols represent the diffusion coefficients of single Cu atoms, as calculated by a combined *ab initio*-mean field model [45].

of MFP shown in Fig. 6, which is at any rate due to a higher stability of the vCu_n complex rather than to a higher mobility. As a matter of fact, the migration energy does decrease in the size range between approximately 50 and 400 atoms (Fig. 5), although this effect is overturned by the strong prefactor decrease. It is also worth highlighting the appearance of "magic" cluster sizes, corresponding to particularly stable configurations, in analogy with what was found for pure vacancy clusters [32]. Such configurations correspond to the complete filling of atomic shells: for instance, at $n = 15$ the 1nn and 2nn shells are completely full, and the same applies at $n = 65$ for all shells from 1nn to 6nn. This effect disappears with increasing temperature because of the progressive loss of vacancy-copper correlations.

The results presented in Fig. 9(a) are not directly comparable with those by Soisson and Fu because of the bias introduced by the AKMC procedure. For this reason, Fig. 9(b) reports the results of an additional set of AKMC simulations, where the diffusion time is recorded also when the vacancy is exploring a pure-Fe environment. Furthermore, the simulation time is correctly rescaled considering the measured fraction of time f_v spent by the vacancy far from solute cluster [Eq. (3)]. Given the heavy computational load required to obtain a good statistic, these simulations are performed also at higher temperatures (up to 900 K), at which the copper clusters (especially the small ones) are rather unstable. In order to keep measuring the diffusion coefficient at constant cluster size, Cu atoms

TABLE III. Fraction of time f_v spent by the vacancy in a pure-Fe environment during the AKMC measurements of the diffusion coefficients shown in Fig. 9(b).

Size	500 K	600 K	750 K	900 K
Cu_{15}	5.2×10^{-9}	2.6×10^{-5}	1.6×10^{-3}	2.3×10^{-2}
Cu_{20}	1.6×10^{-9}	1.2×10^{-5}	4.9×10^{-4}	7.8×10^{-3}
Cu_{30}	5.1×10^{-10}	2.3×10^{-7}	1.5×10^{-4}	2.2×10^{-3}
Cu_{45}	2.8×10^{-11}	1.2×10^{-7}	3.1×10^{-5}	7.7×10^{-4}
Cu_{60}	1.7×10^{-11}	3.0×10^{-9}	7.1×10^{-6}	4.1×10^{-4}
Cu_{90}	–	1.6×10^{-9}	3.1×10^{-7}	1.9×10^{-4}
Cu_{120}	–	1.0×10^{-9}	2.0×10^{-7}	1.6×10^{-4}

lost during the simulation are "manually" replaced back into the cluster at a random position. The bias introduced by this procedure can be regarded as negligible as long as the amount of manual replacements is small, for which reason no clusters smaller than 15 atoms have been simulated. In spite of the computational difficulties, the results shown in Fig. 9(b) are in very satisfactory agreement with those by Soisson and Fu. It is hence possible to confirm with fair confidence that medium-sized copper clusters move faster than small ones. This is due mainly to the strong trapping that reduces drastically the time spent by the vacancy in a pure-Fe environment, especially for large clusters and at low temperatures, as is shown in Table III. The effect progressively disappears with increasing temperature, as expected. This result, combined with the increasing MFPs, suggests that Cu precipitation is mainly driven by direct coarsening of medium-sized clusters, in full agreement with previous investigations [29,31,81]. It is worth mentioning that finite-temperature entropic effects, which are not considered in this model, are known to have an important impact on the vacancy stability in bcc Cu [82]. Consequently, the properties of Cu clusters might differ from the trends emerging from studies based on ground-state properties only.

The properties of small vCu_n clusters ($n \leqslant 4$) are reported in Table IV, alongside the stability and mobility parameters of vacancy-Cu pairs obtained in a previous study [75] based on the same AKMC algorithm. In that case, the *ab initio* vacancy jump frequencies in the dilute-alloy limit were directly implemented. Table IV shows the comparison in terms of

TABLE IV. Diffusion and vacancy-emission parameters of vacancy-copper pairs and clusters obtained by Arrhenius fitting in the temperature range 400–750 K, compared with the results of analogous AKMC simulations with a direct implementation of an *ab initio* multifrequency model [75].

	E^{em} (eV)	τ_0 (10^{-14} s)	E^{mig} (eV)	D_0 (10^{-8} m^2/s)
		Dilute alloy [75]		
v–Cu_1	0.95	1.47	0.73	9.11
		This work		
v–Cu_1	0.87	2.54	0.72	14.6
v–Cu_2	0.93	2.87	0.58	0.83
v–Cu_3	1.01	2.48	0.67	1.52
v–Cu_4	1.12	1.18	0.72	1.68

activation energies and prefactors, obtained by fitting in the temperature range 400–750 K. The results for the v-Cu pair are in good agreement, with the exception of the dissociation energy which is here slightly lower because of a stricter cluster definition (3nn here with respect to the previous 5nn condition [75]). This confirms that the DFT thermodynamic and kinetic properties of the system are correctly transferred to the KMC model. In particular, the flux-coupling tendencies between vacancies and copper atoms (i.e., vacancy drag), which are very sensitive to the migration barriers and are thus difficult to reproduce with simple mathematical models [45], are well caught by the DFT-ANN framework.

It is also interesting to emphasize that the migration barrier of the vCu_2 cluster is considerably lower than that of the vacancy-copper pair, in analogy with the case of two- and three-vacancy clusters with respect to the mono-vacancy [32,83]. Finally, there is a clear difference between the fitted activation energies in Table IV below 750 K, and those above 750 K in Fig. 5. This observation, combined with the other aforementioned changes of behavior across 1100 K, suggests a strong difference in the physical behavior of copper clusters between the low- and the high-temperature range, which is due to the strong vacancy-copper correlations arising at low temperature. The use of DFT as a source of physics for the ANN training ensures that the low-temperature behavior of the system is correctly described, which makes the DFT-ANN approach particularly suitable for low-temperature applications, especially in spin-polarized systems.

B. Copper solubility

The thermal-aging simulations are in satisfactory agreement with the experimental measurements, except for the most dilute alloy (0.6% Cu), where the cluster density is nearly one order of magnitude larger. This clearly shows that the Cu solubility in this model is underestimated. It is well known that, with respect to the Cu solution energy in Fe that can be deduced from the measured solubility limit ($\approx$0.5 eV [29]), the DFT functional here chosen (PBE) predicts a significantly higher value (0.76 eV [47]), even when the entropic contributions to the solution energy are considered [84]. Other GGA functionals such as PW91 [85] or PBEsol [86] yield the same incorrect prediction. On the other hand, less accurate DFT implementations, such as the ultrasoft pseudopotential (USPP) method, do predict values in closer agreement with experiments [47,87], although most likely due to a fortuitous cancellation of errors. The USPP method is known to provide inaccurate predictions of several other properties, such as solute-defect interactions, magnetic moments, and solubility of other transition-metal solutes (e.g., Cr) [47]. For this reason, USPP would not have represented a reliable alternative for the construction of the migration-barrier database. PBE represents thus to date the functional describing at best the ground-state properties of iron alloys.

This mismatch raises two main limitations of the DFT-ANN approach pursued in this work. In first place, the neural network has indeed correctly transferred the alloy properties predicted by DFT to the atomistic simulations, but this does not ensure the full physical reliability of such properties. Second, the tempting possibility of training the neural networks exclusively on kinetic properties (i.e., the migration energies) does not eliminate the necessity of a benchmarking of the thermodynamic properties. In other words, it is still necessary to check the asymptotic behavior of the alloy towards the thermodynamic equilibrium, but this is not easily achievable with a database of migration barriers, where the thermodynamic and kinetic properties are unavoidably mixed up. It seems therefore advisable to split the thermodynamic and kinetic description of the alloy, for instance by distinguishing the two contributions in each energy barrier [18,72]:

$$E_{ij}^{\mathrm{mig}} = E_0^{\mathrm{mig}} + E_i + E_{ij}^{\mathrm{SP}}. \tag{12}$$

Here E_i and E_{ij}^{SP} are the energy of the initial state and the saddle point, respectively, and E_0^{mig} is a reference value (for instance the vacancy migration energy in pure iron). Always relying on DFT data sets, two separate neural networks could therefore be implemented, one targeting the energy difference between initial and final state ($E_i - E_j$), and one focused on the saddle-point energy E_{ij}^{SP}. This approach has been tested in a parallel work [70], with satisfactory results. With such an approach, for instance, the most suitable DFT methods may be chosen to calculate the thermodynamic and kinetic properties separately.

C. Precipitation kinetics

The early stages of precipitation (nucleation, growth, and early coarsening) are very well reproduced by the model. In particular, the matching with the experimental time scale with no adjusting factors is remarkable and represents a clear improvement with respect to the EAM-based work [31]. It should be reminded that this agreement has been achieved as well by including the vacancy formation entropy in the equilibrium concentration [Eq. (4)], which was not considered in the previous work. The comparison with the experimental time scales depends therefore on this parameter, whose value ranges from 4.1 to 4.8 k_{B} according to the most recent DFT calculations [72,74,84]. At any rate, since the EAM results shown in Fig. 8 were rescaled to the equilibrium vacancy concentration assumed in this work, the remarkable improvement in the time evolution is independent of the chosen $S_{\mathrm{v}}^{\mathrm{f}}$.

The precipitation kinetics is therefore correct until the first phase of coarsening. However, the sudden interruption of this phase evidenced in Sec. III C is in clear disagreement with the experimental evidence and goes against the expected physical behavior, since the copper clusters should keep growing in size until a complete phase separation is reached and the residual Cu concentration in the matrix corresponds to the very low solubility limit. As opposed to the expected behavior, in the simulations the coarsening stops at a size of 1000–1500 atoms (1.4–1.6 nm), and there is seemingly an equilibrium between the growth of large clusters and the formation of small ones, sustained by the random emission of a few atoms based on Fig. 7. It is therefore conceivable that the assumption of Cu loss upon vacancy emission should not be valid for large clusters, which should be stable enough, as opposed to the assumptions made in this work.

Besides the lack of a thermodynamic behavior check discussed in the previous section, this unphysical behavior highlights another main limitation of this approach. The DFT cell-size limitation due to computational reasons did not allow for introducing in the database cases of vacancy migration next to large clusters, corresponding exactly to the late stages of the coarsening phase. This deficiency leads unsurprisingly to an incorrect evolution in the late precipitation stage, and clearly limits the validity of this model to the earlier phases. A solution to this limitation is presented in a parallel work [70], where the same DFT database is exploited to infer thermodynamic properties alongside the kinetic ones, and a full DFT-ANN lattice-free interatomic potential is developed. This potential allows for the migration-barriers calculations to be performed in a much more computationally efficient way, extending the database with the missing cases (type III in Fig. 1). It allows as well for a proper thermodynamic investigation aimed at checking the asymptotic equilibrium behavior of the alloy.

In spite of the discussed limitations, the model has been fully successful in transferring the multifold complex properties of FeCu alloys predicted by DFT to higher-scale simulations, well beyond the capabilities of any analytical cohesive model. It therefore represents a solid starting point to build neural-network based tools for the prediction of migration barriers in KMC simulations, fully exploiting the information provided by first-principles methods.

V. CONCLUSIONS

This work presents an original approach for the prediction of unknown point-defect transition rates in kinetic Monte Carlo (KMC) simulations. This approach takes advantage of artificial neural networks (ANNs) to perform nonlinear regression in a data set of *ab initio* migration barriers, replacing interatomic potentials [31] with density functional theory (DFT). The main advantage of this combined DFT-ANN approach is to allow for a full transfer of the alloy thermodynamic and kinetic properties from electronic-structure calculations to atomistic and mesoscopic simulations, which is difficult to achieve with traditional cohesive models. Creating a sufficiently large database of DFT migration barriers is a demanding task in terms of computational load, calling for the best compromise between accuracy, simulation-cell size, and amount of sample cases in the database, while ensuring at the same time an appropriate sampling of the atomic configurations that can be encountered during the simulation. After a careful selection process, 2000 sample configurations were chosen, and the total computational load required amounted to approximately 10 million core hours. The two parallel neural networks trained on this DFT database were shown to provide excellent estimates of unknown migration barriers, at least within the conditions that could be included in the database.

The developed DFT-ANNs were then tested on the simulation of thermal aging in dilute Fe(Cu) alloys through a hybrid atomistic-object KMC model, where the stability and mobility properties of Cu clusters were obtained with separate atomistic KMC simulations driven by the same ANNs. The stronger vacancy-copper binding and kinetic correlations emerging from DFT calculations led to an increased mobility and stability of copper-vacancy clusters, with respect to the previous work based on an EAM interatomic potential [31]. Moreover, both the diffusion coefficient and the mean free path were shown to increase with cluster size until a few hundred atoms, in agreement with previous findings [29]. The role of coarsening of medium- and large-sized clusters in the precipitation process is therefore expected to be even more relevant than what was asserted in previous works [29,31]. The thermal-aging evolution was in good agreement with the experimental one in terms of cluster density and average size; in particular, the match with the experimental time scales was outstanding and did not require any fitting procedure, as opposed to the EAM-based model. Only in the case of the very dilute concentration (0.6 at. % Cu) the density was overestimated. This mismatch showed that the copper solubility predicted by this model is excessively low with respect to reality, accordingly with the erroneous DFT prediction of the solution energy of Cu in Fe. A second limitation of the model was the impossibility of proceeding further than the early coarsening phase, where large clusters (above a thousand atoms) appear. This was due to the DFT cell-size limitation to 250 atoms, which impeded the inclusion of vacancy-migration cases next to larger atoms in the ANN training database. These limitations are addressed in a parallel work [70], where a more sophisticated combination of neural networks, trained over an extended DFT database of cohesive energies and migration barriers, allowed for the development of a full cohesive model which provides a more accurate description of both the thermodynamic and kinetic properties, with excellent results. This DFT-ANN cohesive model effectively boosts and extends the capabilities of DFT, as it greatly reduces the computational load and hence allows for the calculation of larger amounts of reference cases, in larger simulation cells.

In conclusion, the combination of accurate first-principles computations with the regression capabilities of the ANN algorithm can provide a reliable tool to predict migration barriers for KMC simulations as well as in other modeling techniques, while ensuring an accurate description of the multifold properties of the alloy. This study shows that the present-day computational facilities can provide large sets of DFT data, which can be used as data pools for advanced machine-learning treatments, allowing hence for a considerably more extensive application of DFT calculations to higher-scale materials modeling. Moreover, by a simple addition of cleverly chosen samples in the training database, the method can be easily extended to alloys of increasing chemical complexity, with a manageable increase of computational effort but without requiring the cumbersome development of multicomponent interatomic potentials. For this reason, it surely represents a promising support to microstructure evolution simulations of alloys in a wide range of applications and conditions.

ACKNOWLEDGMENTS

The authors acknowledge the financial support from Vattenfall AB, Göran Gustafsson Stiftelse, and the Euratom research and training program 2014–2018 under the Grant Agreement No. 661913 (SOTERIA). This work contributes to the Joint Programme of Nuclear Materials (JPNM) of the European Energy Research Alliance (EERA). The high-performance

computing resources were provided by Électricité de France (R&D) and by the Swedish National Infrastructure for Computing (SNIC). In addition, the authors acknowledge L. Malerba and F. Soisson for their valuable discussions.

[1] J. Allison, D. Backman, and L. Christodoulou, JOM-J. Min. Met. Mat. S. **58**, 25 (2006).
[2] C. S. Becquart and C. Domain, Metall. Mat. Trans. A **42**, 852 (2010).
[3] C. S. Becquart and C. Domain, Phys. Status Solidi B **247**, 9 (2010).
[4] L. Malerba, G. J. Ackland, C. S. Becquart, G. Bonny, C. Domain, S. L. Dudarev, C.-C. Fu, D. Hepburn, M. C. Marinica, P. Olsson, R. C. Pasianot, J. M. Raulot, F. Soisson, D. Terentyev, E. Vincent, and F. Willaime, J. Nucl. Mater. **406**, 7 (2010).
[5] C. S. Becquart, A. Barbu, J.-L. Bocquet, M. J. Caturla, C. Domain, C.-C. Fu, S. I. Golubov, M. Hou, L. Malerba, C. J. Ortiz, A. Souidi, and R. E. Stoller, J. Nucl. Mater. **406**, 39 (2010).
[6] G. R. Odette and R. K. Nanstad, JOM-J. Min. Met. Mat. S. **61**, 17 (2009).
[7] P. Efsing, J. Roudén, and M. Lundgren, in *Effects of Radiation on Nuclear Materials: 25th Volume*, edited by T. Yamamoto (ASTM International, West Conshohocken, PA, 2012), pp. 52–68.
[8] E. Meslin, B. Radiguet, P. Pareige, and A. Barbu, J. Nucl. Mater. **399**, 137 (2010).
[9] M. K. Miller, K. A. Powers, R. K. Nanstad, and P. Efsing, J. Nucl. Mater. **437**, 107 (2013).
[10] P. B. Wells, T. Yamamoto, B. Miller, T. Milot, J. Cole, Y. Wu, and G. R. Odette, Acta Mater. **80**, 205 (2014).
[11] J. P. Wharry and G. S. Was, J. Nucl. Mater. **442**, 7 (2013).
[12] C. Pareige, V. Kuksenko, and P. Pareige, J. Nucl. Mater. **456**, 471 (2015).
[13] A. Chatterjee and D. G. Vlachos, J. Comput.-Aided Mater. Des. **14**, 253 (2007).
[14] A. R. Allnatt and A. B. Lidiard, *Atomic Transport in Solids* (Cambridge University Press, Cambridge, 2003).
[15] G. Henkelman and H. Jónsson, J. Chem. Phys. **111**, 7010 (1999).
[16] O. Trushin, A. Karim, A. Kara, and T. S. Rahman, Phys. Rev. B **72**, 115401 (2005).
[17] N. Castin and L. Malerba, J. Chem. Phys. **132**, 074507 (2010).
[18] H. C. Kang and W. H. Weinberg, J. Chem. Phys. **90**, 2824 (1989).
[19] E. Vincent, C. S. Becquart, and C. Domain, J. Nucl. Mater. **382**, 154 (2008).
[20] E. Vincent, C. S. Becquart, C. Pareige, P. Pareige, and C. Domain, J. Nucl. Mater. **373**, 387 (2008).
[21] F. Soisson, C. S. Becquart, N. Castin, C. Domain, L. Malerba, and E. Vincent, J. Nucl. Mater. **406**, 55 (2010).
[22] R. Ngayam-Happy, P. Olsson, C. S. Becquart, and C. Domain, J. Nucl. Mater. **407**, 16 (2010).
[23] R. Ngayam-Happy, C. S. Becquart, and C. Domain, J. Nucl. Mater. **440**, 143 (2013).
[24] J. M. Sanchez, F. Ducastelle, and D. Gratias, Physica A **128**, 334 (1984).
[25] M. Y. Lavrentiev, R. Drautz, D. Nguyen-Manh, T. P. C. Klaver, and S. L. Dudarev, Phys. Rev. B **75**, 014208 (2007).
[26] M. Y. Lavrentiev, D. Nguyen-Manh, and S. L. Dudarev, Comput. Mater. Sci. **49**, S199 (2010).
[27] C. Pareige, M. Roussel, S. Novy, V. Kuksenko, P. Olsson, C. Domain, and P. Pareige, Acta Mater. **59**, 2404 (2011).
[28] G. Bonny, N. Castin, J. Bullens, A. Bakaev, T. C. P. Klaver, and D. Terentyev, J. Phys.: Condens. Matter **25**, 315401 (2013).
[29] F. Soisson and C.-C. Fu, Phys. Rev. B **76**, 214102 (2007).
[30] O. Senninger, E. Martínez, F. Soisson, M. Nastar, and Y. Bréchet, Acta Mater. **73**, 97 (2014).
[31] N. Castin, M. I. Pascuet, and L. Malerba, J. Chem. Phys. **135**, 064502 (2011).
[32] N. Castin, M. I. Pascuet, and L. Malerba, J. Nucl. Mater. **429**, 315 (2012).
[33] G. Henkelman, B. P. Uberuaga, and H. Jónsson, J. Chem. Phys. **113**, 9901 (2000).
[34] G. Henkelman and H. Jónsson, J. Chem. Phys. **113**, 9978 (2000).
[35] R. C. Pasianot and L. Malerba, J. Nucl. Mater. **360**, 118 (2007).
[36] G. Bonny, R. C. Pasianot, D. Terentyev, and L. Malerba, Philos. Mag. **91**, 1724 (2011).
[37] M. I. Mendelev, S. Han, D. J. Srolovitz, G. J. Ackland, D. Y. Sun, and M. Asta, Philos. Mag. **83**, 3977 (2003).
[38] M. C. Marinica, L. Ventelon, M. R. Gilbert, L. Proville, S. L. Dudarev, J. Marian, G. Bencteux, and F. Willaime, J. Phys.: Condens. Matter **25**, 395502 (2013).
[39] M. S. Daw and M. I. Baskes, Phys. Rev. B **29**, 6443 (1984).
[40] S. Nouranian, M. A. Tschopp, S. R. Gwaltney, M. I. Baskes, and M. F. Horstemeyer, Phys. Chem. Chem. Phys. **16**, 6233 (2014).
[41] C.-C. Fu, J. Dalla Torre, F. Willaime, J.-L. Bocquet, and A. Barbu, Nat. Mater. **4**, 68 (2005).
[42] F. G. Djurabekova, L. Malerba, C. Domain, and C. S. Becquart, Nucl. Instrum. Methods Phys. Res., Sect. B **255**, 47 (2007).
[43] P. Olsson, J. Nucl. Mater. **386-388**, 86 (2009).
[44] S. Huang, D. L. Worthington, M. Asta, V. Ozolins, G. Ghosh, and P. K. Liaw, Acta Mater. **58**, 1982 (2010).
[45] L. Messina, M. Nastar, T. Garnier, C. Domain, and P. Olsson, Phys. Rev. B **90**, 104203 (2014).
[46] J. P. Perdew, K. Burke, and M. Ernzerhof, Phys. Rev. Lett. **77**, 3865 (1996).
[47] P. Olsson, T. P. C. Klaver, and C. Domain, Phys. Rev. B **81**, 054102 (2010).
[48] J. Behler, Int. J. Quantum Chem. **115**, 1032 (2015).
[49] A. P. Bartók and G. Csányi, Int. J. Quantum Chem. **115**, 1051 (2015).
[50] N. Artrith and J. Behler, Phys. Rev. B **85**, 045439 (2012).
[51] N. Artrith, B. Hiller, and J. Behler, Phys. Status Solidi B **250**, 1191 (2013).
[52] O. I. Gorbatov, P. A. Korzhavyi, A. V. Ruban, B. Johansson, and Y. N. Gornostyrev, J. Nucl. Mater. **419**, 248 (2011).
[53] S. Ishino, Y. Chimi, Bagiyono, T. Tobita, N. Ishikawa, M. Suzuki, and A. Iwase, J. Nucl. Mater. **323**, 354 (2003).
[54] A. V. Barashev and A. C. Arokiam, Philos. Mag. Lett. **86**, 321 (2006).

[55] F. Soisson and C.-C. Fu, Solid State Phenom. **139**, 107 (2008).
[56] M. I. Pascuet, N. Castin, C. S. Becquart, and L. Malerba, J. Nucl. Mater. **412**, 106 (2011).
[57] O. I. Gorbatov, I. K. Razumov, Y. N. Gornostyrev, V. I. Razumovskiy, P. A. Korzhavyi, and A. V. Ruban, Phys. Rev. B **88**, 174113 (2013).
[58] V. G. Vaks, F. Soisson, and I. A. Zhuravlev, Philos. Mag. **93**, 3084 (2013).
[59] C. M. Bishop, Rev. Sci. Instrum. **65**, 1803 (1994).
[60] C. M. Bishop, *Neural Networks for Pattern Recognition* (Oxford University Press, Oxford, 1995).
[61] N. Castin, R. Pinheiro Domingos, and L. Malerba, Int. J. Comput. Int. Syst. **1**, 340 (2008).
[62] G. Kresse and J. Hafner, Phys. Rev. B **47**, 558 (1993).
[63] G. Kresse and J. Hafner, Phys. Rev. B **49**, 14251 (1994).
[64] G. Kresse and J. Hafner, J. Phys.: Condens. Matter **6**, 8245 (1994).
[65] P. E. Blöchl, Phys. Rev. B **50**, 17953 (1994).
[66] G. Kresse and D. Joubert, Phys. Rev. B **59**, 1758 (1999).
[67] S. H. Vosko, L. Wilk, and M. Nusair, Can. J. Phys. **58**, 1200 (1980).
[68] P. Olsson, C. Domain, and J. Wallenius, Phys. Rev. B **75**, 014110 (2007).
[69] C. Kittel, *Introduction to Solid State Physics*, 8th ed. (Wiley, New York, 2004).
[70] N. Castin, L. Messina, C. Domain, R. C. Pasianot, and P. Olsson, Phys. Rev. B (to be published).
[71] A. B. Bortz, M. H. Kalos, and J. L. Lebowitz, J. Comput. Phys. **17**, 10 (1975).
[72] L. Messina, M. Nastar, N. Sandberg, and P. Olsson, Phys. Rev. B **93**, 184302 (2016).
[73] P. J. Othen, M. L. Jenkins, and G. Smith, Philos. Mag. A **70**, 1 (1994).
[74] G. E. Lucas and R. Schäublin, Nucl. Instrum. Methods Phys. Res. Sect. B **267**, 3009 (2009).
[75] L. Messina, L. Malerba, and P. Olsson, Nucl. Instrum. Methods Phys. Res. Sect. B **352**, 61 (2015).
[76] S. R. Goodman, S. S. Brenner, and J. R. Low, Metal. Trans. **4**, 2371 (1973).
[77] R. Kampmann and R. Wagner, in *Atomic Transport and Defects in Metals by Neutron Scattering*, edited by C. Janot, W. Petry, D. Richter, and T. Springer (Springer, New York, 1986), p. 76.
[78] J. T. Buswell, C. A. English, M. G. Hetherington, W. J. Phythian, G. D. W. Smith, and G. M. Worrall, *Effects of Radiation on Materials: 14th International Symposium (Volume II)*, edited by N. H. Packan, R. E. Stoller, and A. S. Kumar (American Society for Testing and Materials, Philadelphia, 1990).
[79] M. H. Mathon, A. Barbu, F. Dunstetter, F. Maury, N. Lorenzelli, and C. H. De Novion, J. Nucl. Mater. **245**, 224 (1997).
[80] M. Perez, F. Perrard, V. Massardier, X. Kleber, A. Deschamps, H. de Monestrol, P. Pareige, and G. Covarel, Philos. Mag. **85**, 2197 (2007).
[81] T. Jourdan, F. Soisson, E. Clouet, and A. Barbu, Acta Mater. **58**, 3400 (2010).
[82] P. Erhart, J. Marian, and B. Sadigh, Phys. Rev. B **88**, 024116 (2013).
[83] F. Djurabekova, L. Malerba, R. C. Pasianot, P. Olsson, and K. Nordlund, Philos. Mag. **90**, 2585 (2010).
[84] D. Murali, M. Posselt, and M. Schiwarth, Phys. Rev. B **92**, 064103 (2015).
[85] J. P. Perdew, J. A. Chevary, S. H. Vosko, K. A. Jackson, M. R. Pederson, D. J. Singh, and C. Fiolhais, Phys. Rev. B **46**, 6671 (1992).
[86] J. P. Perdew, A. Ruzsinszky, G. I. Csonka, O. A. Vydrov, G. E. Scuseria, L. A. Constantin, X. Zhou, and K. Burke, Phys. Rev. Lett. **100**, 136406 (2008).
[87] C. Domain and C. S. Becquart, Phys. Rev. B **65**, 024103 (2001).